PHYSICAL REVIEW B **109**, 195201 (2024)

Realizing high phonon anharmonicity in layered Mg_3Sb_2: A temperature-dependent optical phonon study

Minati Tiadi,[1,2] Dillip K. Satapathy,[2,*] and Manjusha Battabyal[1,†]

[1]*International Advanced Research Centre for Powder Metallurgy and New Materials (ARCI), IIT M Research Park, Chennai 600113, India*

[2]*Soft Materials Laboratory, Department of Physics, Indian Institute of Technology Madras, Chennai 600036, India*

(Received 15 November 2023; revised 6 March 2024; accepted 17 April 2024; published 3 May 2024)

The layered compound Mg_3Sb_2 displays remarkable thermoelectric properties at low to moderate temperatures due to its low lattice thermal conductivity, akin to heavier materials like SnSe, PbTe, or Bi_2Te_3. However, the underlying cause of this low lattice thermal conductivity in the lightweight Mg_3Sb_2 remains unclear. Employing temperature-dependent Raman spectroscopy, we have identified the existence of a robust anharmonic interaction between the optical phonon modes in polycrystalline Mg_3Sb_2. Additionally, we have observed a gradual decay of all optical phonons as temperature increases confirming the decrease in lattice thermal conductivity at higher temperatures. The introduction of Li into Mg_3Sb_2 lattice results in a disparity among the crystallographic axes for the phonon modes, intensifying the anharmonic phonon vibrations in $Mg_{2.985}Li_{0.015}Sb_2$ compared to undoped Mg_3Sb_2. The estimated anharmonic constant $\sim 4.5 \times 10^{-4}\,K^{-1}$ for $Mg_{2.985}Li_{0.015}Sb_2$ closely resembles those of other heavier thermoelectric systems, mainly attributed to quasiharmonic volume expansion and anharmonic phonon-phonon interaction. The lattice thermal conductivity estimated from the Raman modes aligns with experimentally measured values, confirming the significant influence of optical phonons on the thermal transport of layered Mg_3Sb_2. These findings offer a comprehensive exploration of the interplay between optical phonon modes and the origins of substantial phonon anharmonicity in the lightweight polycrystalline Mg_3Sb_2 system.

DOI: 10.1103/PhysRevB.109.195201

I. INTRODUCTION

Layered polycrystalline Mg_3Sb_2 has garnered significant interest as a potential thermoelectric (TE) material for low to moderate temperature applications due to its cost effectiveness, environmental friendliness, and the ability to form both *p*- and *n*-type Mg_3Sb_2 through efficient doping. For a system to achieve higher TE efficiency (zT), it is crucial to lower its lattice thermal conductivity, as outlined in the equation $zT = \sigma S^2 T/(\kappa_e + \kappa_{lattice})$. Here, σ, S, $\kappa_{lattice}$, and κ_e respectively denote the electrical conductivity, Seebeck coefficient, lattice thermal conductivity, and electronic thermal conductivity of the samples at absolute temperature T [1]. To enhance zT in a TE system, it is vital to have higher values for S and σ, while reducing κ_e and $\kappa_{lattice}$. In a TE semiconductor, $\kappa_{lattice}$ predominantly influences thermal conductivity and hence it is very important to investigate the $\kappa_{lattice}$ of a TE system. Although first-principle band structure calculations have provided a predictive understanding of electronic transport properties in material design, achieving a quantitative microscopic comprehension of thermal transport in the layered Mg_3Sb_2 system remains a challenging endeavor.

The layered Mg_3Sb_2 compound is categorized as a Zintl compound and boasts a hexagonal crystal structure with P-3m1 space group. It consists of an anionic $[Mg_2Sb_2]^{2-}$ layer nestled between two cationic ${Mg_2}^{2+}$ layers. The bond between Mg and Sb within the $[Mg_2Sb_2]^{2-}$ layer is covalent, whereas an ionic bond is present between the $[Mg_2Sb_2]^{2-}$ and ${Mg_2}^{2+}$ layers. The two different Mg atoms in Mg_3Sb_2 occupy the octahedral sites of the $[Mg_2Sb_2]^{2-}$ layer and the tetrahedral site within the $[Mg_2Sb_2]^{2-}$ slabs [2]. A key feature of Mg_3Sb_2 is its notably low lattice thermal conductivity, contributing to the enhancement of its zT values. Remarkably, despite being significantly lighter in weight compared to SnSe, PbTe, ZnSb, and Bi_2Te_3, Mg_3Sb_2 demonstrates relatively lower thermal conductivity [3–10]. The lattice thermal conductivity, approximately $\sim 1.3\,W/mK$, achieved for *p*-type undoped Mg_3Sb_2, is comparable to that of Bi_2Te_3, despite the latter having a mass approximately 2.5 times heavier than Mg_3Sb_2, or even with barium clathrates characterized by a complex crystal structure. This defies the common mass law: $\kappa_{lattice} \propto M^{-1}$ [3,7,11]. Moreover, $\kappa_{lattice}$ decreases when lighter atoms like Li/Na replace Mg, contradicting the mass law once again [7]. This suggests the existence of a concealed mechanism that significantly restrains phonon propagation in lightweight Mg_3Sb_2 compounds.

While considerable research has been conducted on the electronic properties of undoped and doped Mg_3Sb_2, there are few in-depth investigations on the phonon anharmonicity and lattice thermal conductivity to date [5,6,12–15]. Understanding the lattice dynamics, phonon anharmonicity, and their relationship with $\kappa_{lattice}$ are critical for enhancing TE properties [12,13,16]. Ma *et al.* compared the experimental data with the calculated Fourier electron density maps generated by single-crystal data and suggested that in the case of *p*-type

---

[*] dks@iitm.ac.in

[†] manjusha.battabyal@gmail.com

Mg_3Sb_2, there are Mg vacancies at both anionic and cationic layers, that affects the phonon vibrational modes [13]. The recent study on the density functional studies of the Mg_3Sb_2 by Wu *et al.* reveals the change in chemical bond around Sb atoms due to cationic site defects, that leads to high anharmonicity in the Mg_3Sb_2 lattice resulting in the reduction of lattice thermal conductivity [12]. However, the experimental investigations on the lattice anharmonicity of layered Mg_3Sb_2 are not matured to date.

Raman spectroscopy, an adaptable technique encompassing the interaction between light and matter, serves as an effective tool for studying phonon anharmonicity in materials. It offers insights into vibrational properties arising from a material's crystal structure, thermal expansion, chemical composition, and bonding [17,18]. Phonons, carrying information about atomic and lattice vibrations, are strongly impacted by structural imperfections such as defects and impurities. Consequently, Raman spectroscopy stands as a robust method to extract details on defects, phases, crystallinity, inhomogeneities, and anharmonicity in materials. Given that Raman spectroscopy provides collective information on phonon vibrational modes, a comprehensive exploration of all the Raman modes in a system allows estimation of phonon/lattice thermal conductivity. Temperature-dependent Raman modes offer substantial insights into lattice vibrational properties. Therefore, alteration in Raman peak position and linewidth with temperature yield comprehensive information about lattice anharmonicity [18].

In this study, we conducted an investigation into the temperature-dependent behavior of various optical phonon modes in both polycrystalline undoped and Li-doped Mg_3Sb_2. We employed both temperature- and angle-dependent Raman spectroscopy techniques to delve into the phonon anharmonicity in the Mg_3Sb_2 system. Our findings revealed that Li doping induced alterations in the symmetry axis of the optical phonon modes, leading to an enhancement in phonon anharmonicity. The contributions from both three-phonon and four-phonon processes influencing the lattice thermal conductivity in the layered Mg_3Sb_2 are confirmed. Our study presents detailed examinations of the temperature-dependent optical phonon modes in polycrystalline undoped and Li-doped Mg_3Sb_2 within the temperature range 173–503 K. We confirmed the existence of low lattice thermal conductivity in Mg_3Sb_2, manifested through the phonon anharmonicity and decay of optical phonon modes. Additionally, our investigation has unveiled a correlation between the estimated lattice thermal conductivity values derived from optical phonon modes and the values obtained through experimental measurement. This correlation implies the significant role of optical phonon vibration in the thermal transport of layered thermoelectric materials.

II. EXPERIMENTS

The synthesis route of undoped and Li-doped Mg_3Sb_2 is detailed in our previous report, which involves ball milling of raw materials in an inert gas atmosphere followed by vacuum hot pressing [7]. The obtained hot-pressed samples are of cylindrical in size and the density of the hot-pressed solid samples is found to be ~99% of the theoretical density. The in-depth microstructure of the samples was carried out using a high-resolution transmission electron microscope (JEOL, JEM-2100plus). The optical phonon modes of the obtained samples were investigated using the HORIBA LabRAM confocal micro-Raman system equipped with a liquid-nitrogen-cooled CCD camera and a laser source of 632-nm wavelength was used for probing the samples. The laser beam spot size was ~1 μm during measurements [19,20]. The room-temperature Raman spectra are collected at different laser power starting from ~0.51 mW to 6.54 mW. The resolution of Raman measurement was $1\ \mathrm{cm}^{-1}$, and the spectra were collected in a $40\ \mathrm{cm}^{-1}$ to $200\ \mathrm{cm}^{-1}$ wavenumber range with 20 s acquisitions time and grating line 1800 lines/inch. A 50X objective was used for all types of Raman scattering experiments. A laser flash apparatus (Netzsch, LFA 457) is employed for temperature-dependent thermal diffusivity experiments, and a differential scanning calorimetry (Netzsch, DSC404) was used to measure high-temperature specific heat capacity (C_p). The low-temperature C_p of the samples was carried out using the Physical Properties Measurement System (PPMS, Quantum Design, USA). The error in the C_p measurements is calculated to be ~7%. A dilatometry (Dil 402 supreme, Netzsch) is used to probe the linear thermal expansion coefficient of the samples between 300 to 675 K temperature range.

III. RESULTS AND DISCUSSIONS

The Mg_3Sb_2 has a layered crystal structure, where anionic $[Mg_2Sb_2]^{2-}$ layer (Mg in the anionic layer will be labeled as Mg2 in the remaining part of the text) is sandwiched between two cationic Mg^{2+} layers (Mg in the cationic layer will be noted as Mg1), and is visualized in Fig. 1(a). The x-ray diffraction studies as depicted in Fig. 1(b) reveal the presence of Mg_3Sb_2 as major phase in both undoped and Li-doped Mg_3Sb_2. A minute quantity ($\sim 2-3\%$) of Sb is found to be present in the samples [7]. The nanocrystalline nature of the samples is also confirmed from the high-resolution TEM (HRTEM) images as shown in Figs. 1(c)–1(e). The lattice fringes from (011), (012), and (110) planes are apparent and lattice spacing are estimated to be 0.346, 0.265, and 0.227 nm, respectively, those correspond to the $\alpha - Mg_3Sb_2$ phase having hexagonal crystal structure [7]. The selected area electron diffraction (SAED) patterns obtained from Mg_3Sb_2 lattice confirms the nature of the sample [refer to Fig. 1(e)]. It can be observed from Figs. 1(a) and 1(f) that three different bonds exist between Mg and Sb atoms, namely: (i) interlayer Mg1–Sb bond (d1), (ii) tilted Mg2-Sb bond (d2), and (iii) vertical Mg2-Sb bond (d3). It is worth noting that the chemical strength of the three different bonds is different from each other and follows the d1 > d2 > d3 order. In the case of Mg_3Sb_2, Mg1, Mg2, and Sb are nonequivalent atoms having completely different chemical states. After confirming the crystalline nature of the processed samples, we now turn to discuss the optical modes present in the layered Mg_3Sb_2 system. It is mentioned earlier that the Mg1 occupying between two $[Mg_2Sb_2]^{2-}$ anion slabs is octahedrally coordinated with Sb, whereas Mg2 is tetrahedrally coordinated with Sb atoms [21]. The primitive cell of Mg_3Sb_2 contains five atoms having P-3m1 space group and $D_{3d}(-3m)$ point group. From the

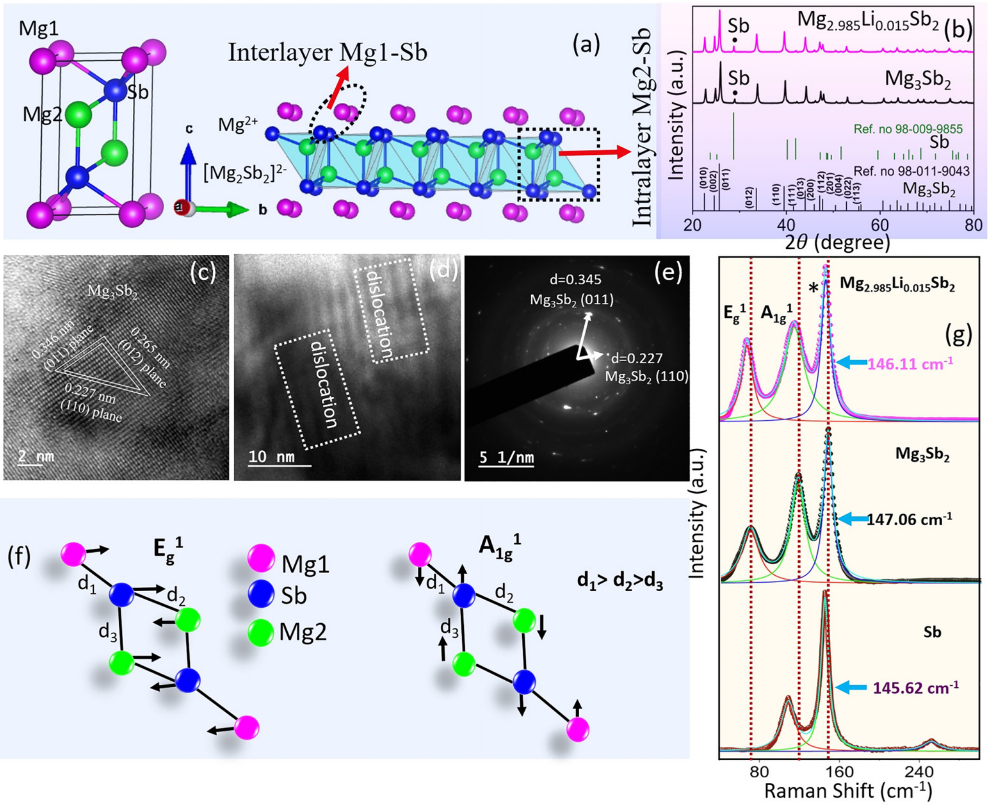

FIG. 1. (a) The unit cell of layered Mg_3Sb_2, and the Mg1-Sb interlayers inside the unit cell, (b) x-ray diffraction pattern of undoped, Li-doped Mg_3Sb_2, the peaks corresponding to elemental Sb are marked with a blue solid circle. [(c)–(e)] High-resolution transmission electron microscopy images showing the crystalline nature of Mg_3Sb_2, dislocation present in the system, and selective area electron diffraction pattern confirming the Mg_3Sb_2 phase, and (f) transverse and longitudinal phonon modes in Mg_3Sb_2. (g) Raman spectra of pure Sb, Mg_3Sb_2 and $Mg_{2.985}Li_{0.015}Sb_2$ at 300 K.

group theory study, Mg_3Sb_2 is expected to have 15 optical phonon vibrational modes among which three are acoustic modes and twelve are optical modes [22]. The optical phonon modes "Γ_{vib}" of Mg_3Sb_2 system can be written as

$$\Gamma_{\text{vib}} = 2\text{E}_{\text{g}}(R) + 2\text{E}_{\text{u}}(I) + 2\text{A}_{1\text{g}}(R) + 2\text{A}_{1\text{u}}(I), \qquad (1)$$

where R and I, respectively represent the Raman-active and IR-active modes [23]. E_g and E_u are transverse phonon modes, which are doubly degenerate, whereas A_{1g} and A_{1u} represent longitudinal phonon modes. For Raman active modes, the Raman tensors are as follows [24]:

$$\text{A}_{1\text{g}} = \begin{pmatrix} a & 0 & 0 \\ 0 & a & 0 \\ 0 & 0 & b \end{pmatrix},$$

$$\text{E}_{\text{g}}^1 = \begin{pmatrix} c & 0 & 0 \\ 0 & -c & d \\ 0 & d & 0 \end{pmatrix},$$

$$\text{E}_{\text{g}}^2 = \begin{pmatrix} 0 & -c & -d \\ -c & 0 & 0 \\ -d & 0 & 0 \end{pmatrix}, \qquad (2)$$

Here, a, b, c, and d are the components of the Raman tensor. The nonzero off-diagonal Raman tensor components in the E_g mode play a vital role in differentiating the E_g mode from the A_{1g} mode.

The Raman spectra recorded at 300 K for Sb, undoped Mg_3Sb_2, and Li-doped Mg_3Sb_2 ($Mg_{2.985}Li_{0.015}Sb_2$) are depicted in Fig. 1(g), that confirms the presence of three distinct Raman modes at 69, 117, and 147 cm^{-1} in undoped Mg_3Sb_2 and at 68, 114, and 146 cm^{-1} in Li-doped Mg_3Sb_2. Three Raman modes have been identified for elemental antimony (Sb) powder at 108.96, 145.62, and 252.20 cm^{-1}. Notably, the only mode observed at 145.62 cm^{-1} in Sb closely lies to the 147 cm^{-1} mode observed for Mg_3Sb_2 system. It is important to mention that although there are few studies on the Raman modes of layered materials, there is hardly any report so far on the Raman modes observed in polycrystalline Mg_3Sb_2 [12,13]. However, the room-temperature Raman spectra of single crystalline Mg_3Sb_2 are reported by Jin *et al.*, which shows the presence of two transverse and one longitudinal phonon modes [25]. On the other hand, recent reports on theoretical studies of the Raman modes in *p*-type Mg_3Sb_2 reveal that two distinct Raman modes at 69 and 117 cm^{-1} correspond to E_g^1 and A_{1g}^1 respectively. The third peak around 147 cm^{-1} is a debatable peak that can arise from secondary Sb present in our samples or it can be considered as Raman forbidden IR peak [12,13]. The appearance of the forbidden Raman peak in *p*-type Mg_3Sb_2 may be

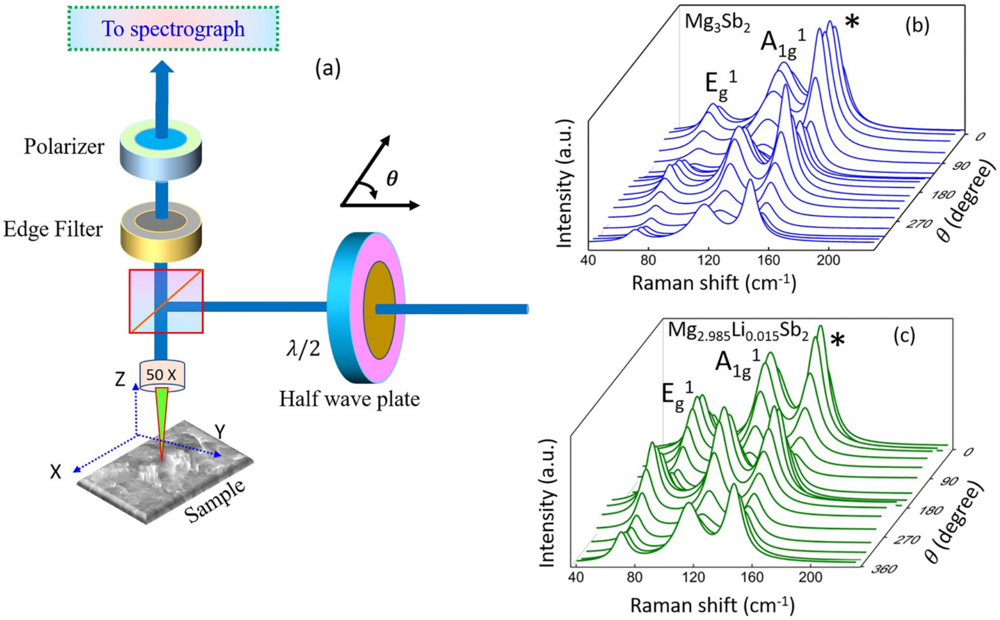

FIG. 2. (a) Schematic of the polarized Raman spectroscopy experimental set-up. The 3D plot showing the intensity variation of E_g^1, A_{1g}^1, and forbidden Raman modes with respect to polarized angle for (b) Mg_3Sb_2, and (c) $Mg_{2.985}Li_{0.015}Sb_2$ samples.

due to the change detection of the zone-edged acoustic phonon modes (the acoustic branches extending to the A point) [26]. As can be observed from Fig. 1(g), it is interesting to note that compared to E_g^1 and A_{1g}^1 peaks, the peak shift for this particular peak is minimal in Li-doped sample, that lies within the experimental error of the measurements. The schematics of E_g^1 and A_{1g}^1 of layered Mg_3Sb_2 is represented in Fig. 1(f). It can be envisaged from Fig. 1(g) that the Raman modes shift towards lower frequency when Li is doped at the Mg1 site of Mg_3Sb_2 lattice. This indicates the comparatively lower energy for optical phonon modes in doped samples compared to that for undoped Mg_3Sb_2. The low energy of the optical phonon modes in the Li-doped Mg_3Sb_2 can be understood by taking into account its individual bond strength. When Li is doped at the Mg1 site of Mg_3Sb_2, there is a change in the bond length due to the different ionic radii of Li and Mg. Since the ionic radius of Li is larger than that of Mg [7], the bond length increases when Li-doped Mg_3Sb_2, which will eventually lead to the decrease in bond strength, and hence softening of the optical phonon modes will be expected in Li-doped Mg_3Sb_2 compared to that of undoped Mg_3Sb_2 [20]. The softening of the phonon modes will eventually lead to the decrease in lattice thermal conductivity in $Mg_{2.985}Li_{0.015}Sb_2$, which will be discussed in the later part of the text. Next, we have carried out room-temperature polarized Raman spectroscopy to investigate Li-doping effect on the crystallographic axes of the optical phonon modes in Mg_3Sb_2 and is visualized in Fig. 2. For the polarized Raman spectroscopy experiment, the polarization of the incident laser light is carried out in a horizontal direction and the analyzer is fitted near the mouth of the spectroscope to properly analyze the Raman signals from a parallel layout. The angle-dependent Raman spectra are perceived by rotating the polarizer and the analyzer direction is set parallel with the excitation polarization direction [Fig. 2(a)]. A series of angle-dependent Raman spectra are collected under parallel configuration with different "θ" values and are depicted in Figs. 2 and 3. It can be noticed from Figs. 2(b) and 2(c), and 3(a) and 3(b) that peak intensities of E_g^1 and A_{1g}^1 modes exhibit strong angle dependence as demonstrated by the contour color map under parallel-polarized configuration. Figures 3(d) and 3(e) reveals that both the Raman modes are having two-fold symmetry. The twofold symmetry is a signature for anisotropy nature of Mg_3Sb_2 [27]. From the polarized Raman data, the symmetry axis of the Raman modes is determined by fitting the experimental data according to the equation: $I \propto d^2 \sin^2 2(\theta + \theta_0)$, where θ is the polarized angle, θ_0 is the starting angle, and I is the intensity of the Raman modes [28,29]. The variable "d" is related to the magnitude of the Raman tensor as discussed elsewhere [29]. The fitting of the polarized Raman modes is depicted in Fig. 3(c). As shown in Fig. 3(d), the symmetry axes of all the optical phonon modes for undoped Mg_3Sb_2 are found to be at 40 degree. But in case of Li-doped Mg_3Sb_2, the symmetry axes for E_g^1 and A_{1g}^1 modes are at 60 and 40 degree, respectively [see Fig. 3(e)]. This means that Li-doping in Mg_3Sb_2 lattice alters the symmetry axis of the transverse optical phonon modes without changing the symmetry line of the longitudinal mode. The deviation of the symmetry lines for E_g^1 and A_{1g}^1 modes in Li-doped Mg_3Sb_2 can indeed be attributed to change in bond strength due to Li doping at the Mg1 site. It can also be noticed that the symmetry axis of the Raman peak at $147\,\mathrm{cm}^{-1}$ changed from 40 degree in undoped Mg_3Sb_2 to 20 degree in Li-doped Mg_3Sb_2. Here it can be stated that if the peak at $147\,\mathrm{cm}^{-1}$ would have appeared from secondary Sb phase, then the symmetry axis would not have changed in the Li-doped sample. Hence, the third peak at $147\,\mathrm{cm}^{-1}$ may be considered a Raman forbidden IR peak arising from Mg_3Sb_2 lattice [12,25]. This presence of this Raman forbidden peak is also observed in *p*-type Mg_3Sb_2 when there is no secondary Sb is present [12,13]. The different symmetry lines of the

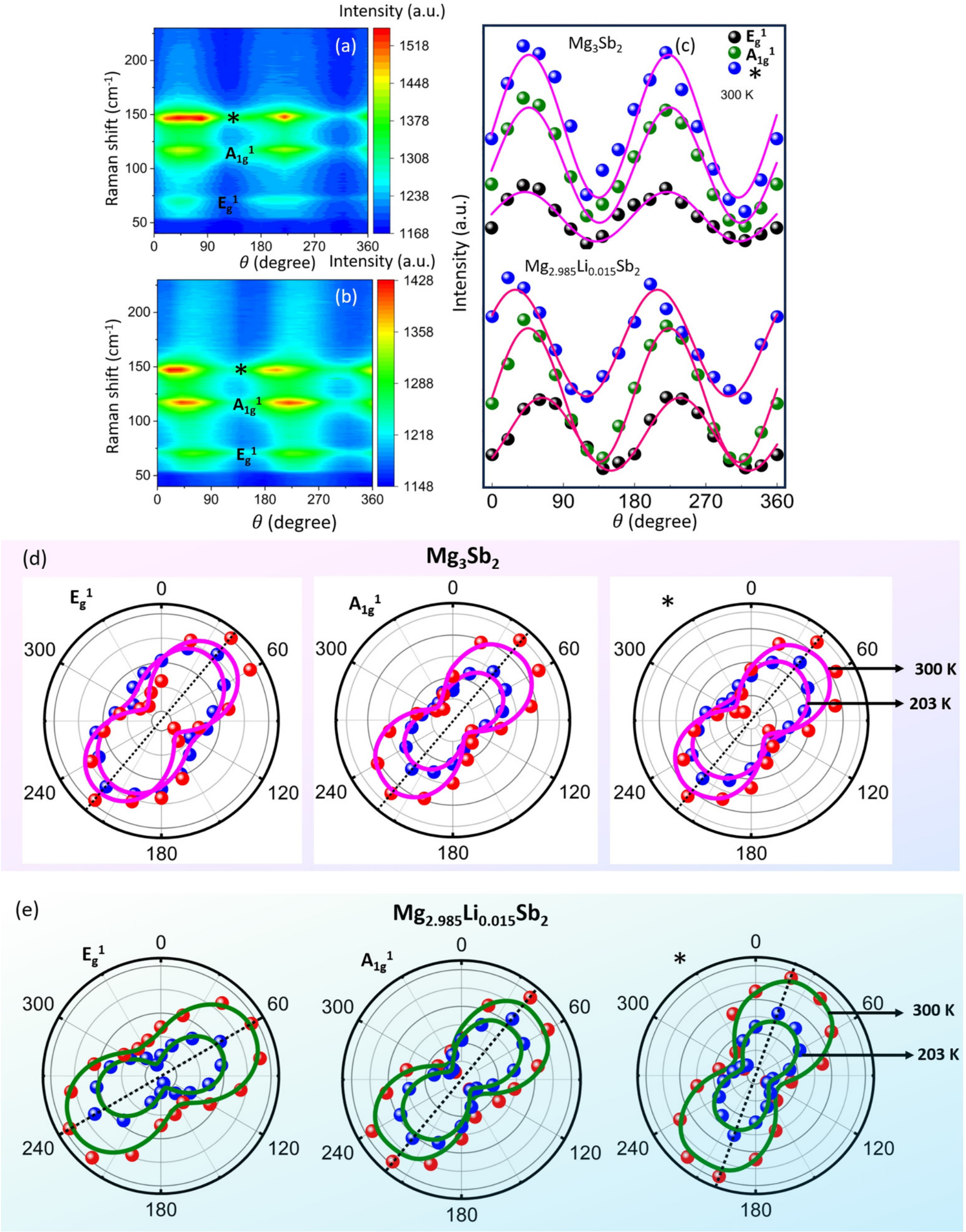

FIG. 3. The contour plot showing the angular dependence of the Raman intensity for all the Raman modes in the parallel-polarized configuration for (a) Mg_3Sb_2, and (b) $Mg_{2.985}Li_{0.015}Sb_2$ at 300 K. (c) The fitting of the polarized Raman data corresponding to $I \propto d^2\sin^2 2(\theta + \theta_0)$ relation, the solid points are the measured data and the line represents the fitted curve. The polarized Raman spectroscopy data along with fitted curve at 203 and 300 K for (d) Mg_3Sb_2, and (e) $Mg_{2.985}Li_{0.015}Sb_2$ samples. The red and blue data points in (d) and (e) represent the polarized Raman data at 300 and 203 K respectively. The lines in (d) and (e) represent the fitted curve according to $I \propto d^2\sin^2 2(\theta + \theta_0)$ relation.

Raman modes in Li-doped Mg_3Sb_2 will have a pronounced effect on its lattice anharmonicity and thermal conductivity [19,20]. To confirm whether temperature has any effect on the crystalline symmetry axis, we have carried polarized Raman spectroscopy at 203 K and is depicted in Figs. 3(d) and 3(e). It can be observed that the crystalline symmetry axis remains unaltered at 203 K. From the polarized Raman spectroscopy experiment on undoped and doped Mg_3Sb_2, it can be concluded that compared to thermal energy, the symmetry axis of the optical phonon modes in polycrystalline Mg_3Sb_2 is directly related to the doping element. The different axis for the optical phonon modes in $Mg_{2.985}Li_{0.015}Sb_2$ is due to the change in the bond length and bond strength of the phonon modes as a result of Li-doping at the Mg1 site of Mg_3Sb_2. This change in symmetry axis of the optical phonons will lead to more phonon anharmonicity in the Li-doped Mg_3Sb_2, which will be detailed here.

After studying the alterations in the symmetry axis of optical phonon modes within Mg_3Sb_2 caused by temperature changes and Li doping, our investigation delved into comprehending the temperature-dependent evolution of peak shifts and the full-width-half-maxima of these optical phonon modes and their impact on lattice thermal conductivity. Raman spectra were recorded from Mg_3Sb_2 and

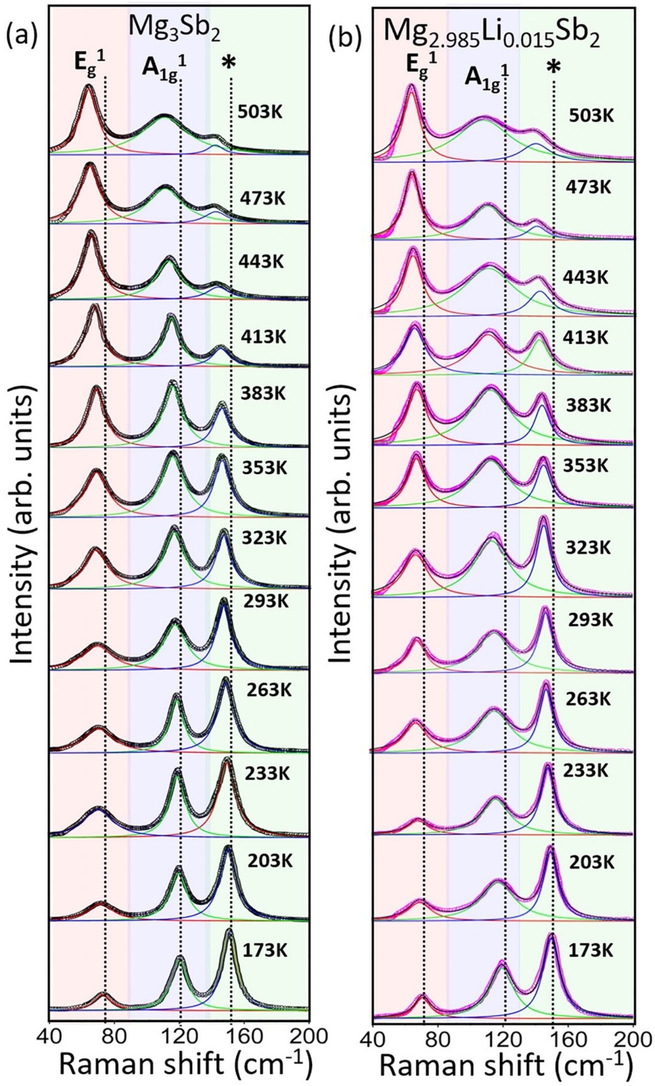

FIG. 4. [(a),(b)] The temperature-dependent Raman spectra of Mg_3Sb_2 and $Mg_{2.985}Li_{0.015}Sb_2$ sample plotted from 173 to 503 K. For better visualization, the Raman spectra are plotted at 30 K interval.

$Mg_{2.985}Li_{0.015}Sb_2$ within the temperature range 173–503 K, at temperature intervals of 30 K, and are depicted in Figs. 4(a) and 4(b). All the three optical phonon modes, namely E_g^1, A_{1g}^1 and Raman forbidden IR modes were consistently observed in both undoped and doped samples across the investigated temperature range. At 173 K, the peak positions of E_g^1, A_{1g}^1, and Raman forbidden IR modes in undoped Mg_3Sb_2 were determined to be at 72.9, 120.3, and 150.4 cm^{-1} respectively, while for the $Mg_{2.985}Li_{0.015}Sb_2$ sample, these modes appeared at 70, 117.3, and 149.5 cm^{-1}, respectively. Figures 4(a) and 4(b) illustrate that the Raman modes of both undoped and Li-doped Mg_3Sb_2 gradually shift towards lower wavenumbers as the temperature increases from 173 to 503 K. This shift indicates a reduction in the vibrational energy of the optical phonons with rising temperature, likely due to an increase in bond length (d1, d2, and d3) as shown in Fig. 1(f), subsequently weakening the bonds and necessitating less energy to excite the optical phonon modes. A noteworthy observation from the temperature-dependent Raman spectroscopy is the variation in intensity, peak position, and full width at half-maxima (FWHM) of these modes with temperature. While the intensity of the E_g^1 mode increases, the A_{1g}^1, and Raman forbidden IR modes display a decrease in intensity with rising temperature. Additionally, the FWHM of all modes consistently increases with temperature. This simultaneous decrease in intensity of the A_{1g}^1 and IR modes and the increase in FWHM of all modes at higher temperatures indicate phonon decay or softening of the A_{1g}^1, and Raman forbidden IR modes, resulting in a more pronounced E_g^1 mode at higher temperatures [19]. The decrease in intensity of E_g^1 and A_{1g}^1 modes in undoped and doped Mg_3Sb_2 compared to the E_g^1 mode might be attributed to the distinct thermal expansion of the chemical bonds corresponding to E_g^1 and A_{1g}^1 modes [30]. The lower phonon energy of A_{1g}^1 and IR modes confirm the phonon decay, suggesting a decrease in lattice thermal conductivity with rising temperatures.

The temperature-dependent lattice thermal conductivity can be better understood by examining the changes in peak position and FWHM of the Raman modes with temperature [31,32]. Previous studies show that the red shift of the Raman peak position with temperature is due to the combined contributions arising from the quasiharmonic volume expansion and anharmonic phonon-phonon interaction, where as change in FWHM is due to the anharmonic phonon-phonon interactions only [31,33]: Accordingly, the temperature-dependent Raman peak shift [$\omega(T)$] and FWHM [$\Gamma(T)$] for our system can be expressed as

$$\omega(T) = \omega_0 + \Delta\omega_j(T)_V + \mathrm{A}\left[1+\frac{2}{e^x-1}\right] + \mathrm{B}\left[1+\frac{3}{e^y-1}+\frac{3}{(e^y-1)^2}\right], \tag{3}$$

$$\Gamma(T) = \Gamma_0 + \mathrm{C}\left[1+\frac{2}{e^x-1}\right] + \mathrm{D}\left[1+\frac{3}{e^y-1}+\frac{3}{(e^y-1)^2}\right]. \tag{4}$$

In Eq. (3), the second term $\Delta\omega_j(T)_V$ is the peak shift corresponding to quasiharmonic volume expansion. The third term in Eq. (3) and second term in Eq. (4) correspond to the contribution due to anharmonic three-phonon interactions, whereas the last term in Eqs. (3) and (4) represent the four-phonon interactions. The contribution due to quasiharmonic volume expansion to the frequency shift can be expressed by the following equation [18,33]:

$$\Delta\omega_j(T)_V = \omega_o\left[exp\left(-\gamma\int_0^T \beta(T)dT\right)-1\right]. \tag{5}$$

Here, γ is the Grüneisen parameter determined from the experimental lattice thermal conductivity data of the samples. Here $\beta(T) = (1/V)dV/dT$ is the volume expansion coefficient and is calculated by fitting volume as a function of temperature as discussed in the literature [18,33,34]. In Eqs. (3) and (4), the variables x and y are expressed as $x = \frac{hc\omega_0}{2k_BT}$ and $y = \frac{hc\omega_0}{3k_BT}$, where ω_0 signifies the intrinsic frequency of the optical phonon mode and Γ_0 denotes the peak widening attributed to disorder and boundary scattering. Notably, A, B, C, and D are recognized as anharmonic

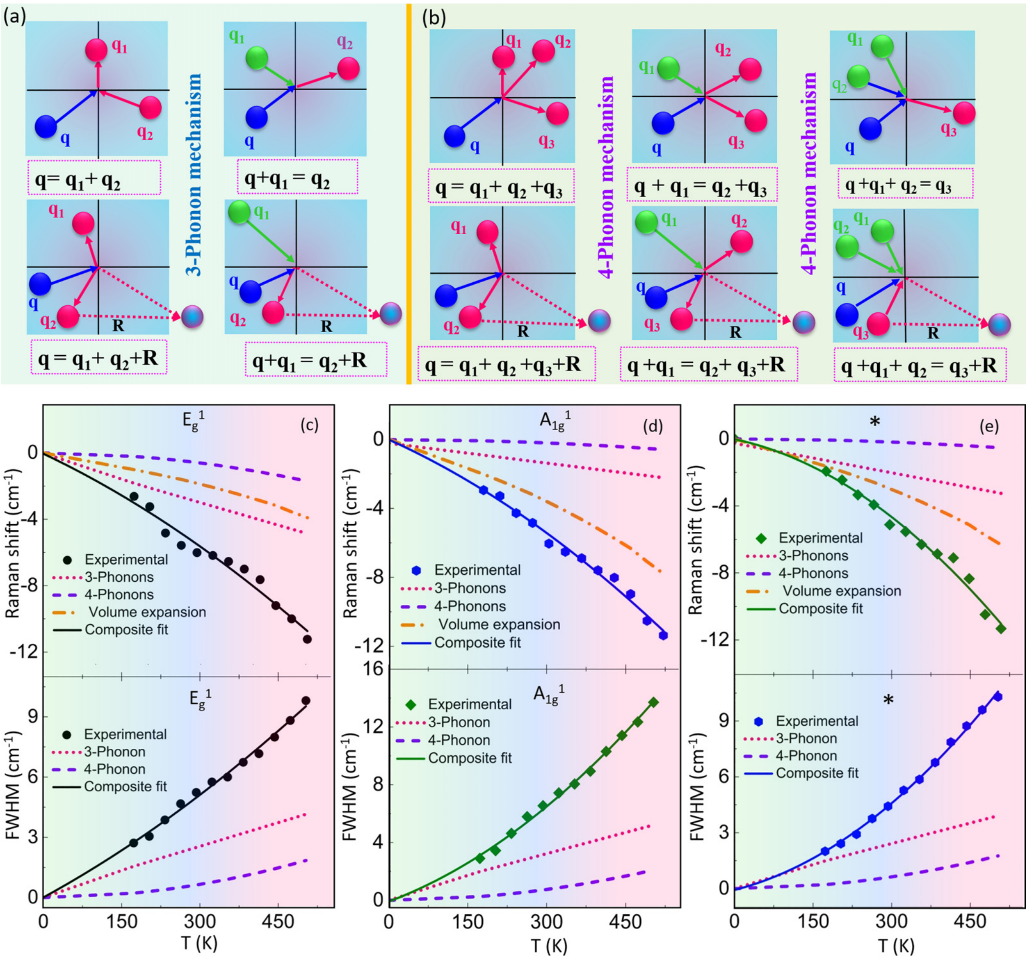

FIG. 5. Schematic showing (a) three phonon scattering and (b) four phonon scattering mechanisms. (c)–(e) represent the anharmonic contributions due to three-phonon, volume expansion and four-phonon to the Raman peak shift, and three-phonon and four-phonon contributions to the FWHM of Raman peaks in Mg_3Sb_2 and $Mg_{2.985}Li_{0.015}Sb_2$.

constants due to phonon-phonon coupling, with h, c, and k_B representing Planck's constant, the speed of light, and the Boltzmann constant, respectively. The estimation of anharmonicity contribution due to thermal expansion, three-phonon, and four-phonon scatterings is derived from the fitting of temperature-dependent Raman peak shift using Eq. (3) and are plotted in Figs. 5(c)–5(e). The three-phonon and four-phonon anharmonic contribution are calculated from the full width at half maximum (FWHM) employing Eq. (4), and are plotted in Figs. 6(a)–6(c). The anharmonic contribution curves in Figs. 5 and 6 depict the best-fit lines along with the recorded data points in the temperature span of 173 to 503 K for both undoped and Li-doped Mg_3Sb_2 utilizing Klemens's model [16,35,36]. Since transverse and longitudinal optical phonon modes possess different velocities, their anharmonicity varies accordingly [21]. Anharmonicity serves as a crucial mechanism responsible for the low lattice thermal conductivity within a system. The anharmonicity calculated from FWHM data using Eq. (4), confirms the prevalence of the three-phonon process in both undoped and Li-doped Mg_3Sb_2 samples. This underscores the significant responsibility of the three-phonon process for the anharmonic lattice thermal conductivity in the Mg_3Sb_2 system. It is notable that there is also a substantial contribution from four-phonon coupling to the phonon anharmonicity of Mg_3Sb_2, whereas in other layered systems like Bi_2Te_3, only three-phonon coupling contributes to the phonon anharmonicity [20]. The estimations of anharmonic contributions, depicted in Fig. 5 conclude that volumetric quasi-anharmonicty, three-phonon and four-phonon anharmonic coupling processes influence the phonon anharmonicity in Mg_3Sb_2, resulting in higher anharmonicity. A similar observation on four-phonon and volumetric contributions to increased phonon anharmonicity is reported for the SnSe single crystal, demonstrating ultralow lattice thermal conductivity [33]. Reducing lattice thermal conductivity in a thermoelectric system significantly contributes to enhancing its thermoelectric efficiency [7,10,37].

As mentioned earlier, the reduced lattice thermal conductivity in the Mg_3Sb_2 system can be realized through its volumetric expansion and phonon anharmonicity. The anharmonic coefficients (α_C) are signatures of phonon anharmonicity and can be estimated from Raman modes as well as from heat capacity. It is known that the anharmonicity of a lattice is the main cause for the shifting and broadening of Raman peaks. The shifting of the peak position and the increase in FWHM of the Raman modes with an increase in temperature indicate more phonon anharmonicity in the lattice at higher temperatures. As per quasiharmonic approximation

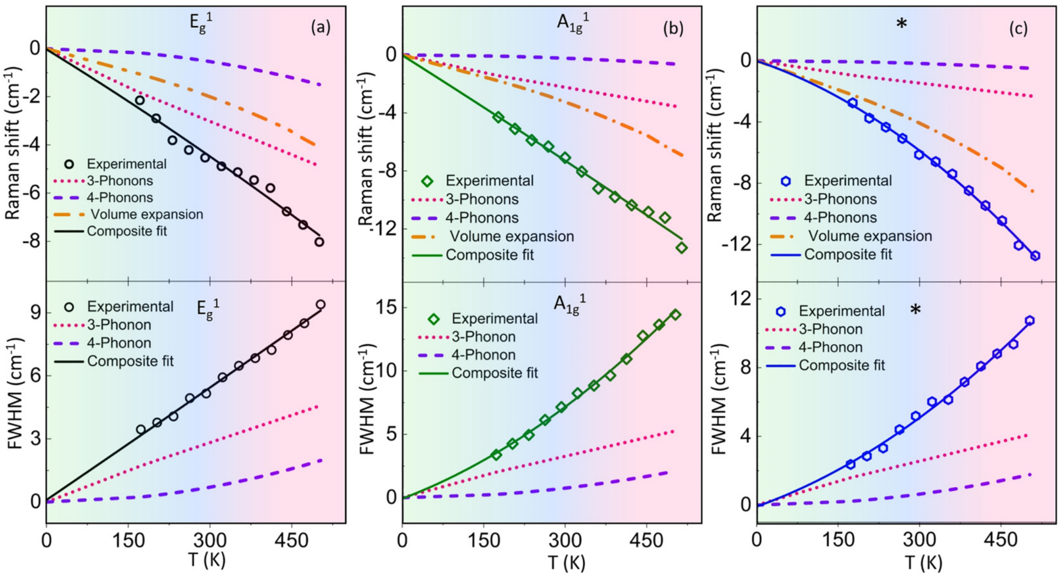

FIG. 6. The anharmonic contributions due to three-phonon, volume expansion and four-phonon to the Raman peak shift, and three-phonon and four-phonon contributions to the FWHM of Raman peaks in Mg_3Sb_2 and $Mg_{2.985}Li_{0.015}Sb_2$ are displayed in (a), (b) and (c).

(qh), the phonon frequency depends solely on volume, and hence, the temperature-dependent lattice dynamics is approximated by the harmonic normal modes $F_{qh}(T, V)$ with phonon frequencies that are shifted due to the thermal expansion [38]. For strongly anharmonic crystals such as SnSe, it was shown that the total free energy F(T, V) includes other contributions arising from the three-phonon and four-phonon processes, viz., $F_3(T, V)$ and $F_4(T, V)$ in addition to $F_{qh}(T, V)$ in addition to the volumetric thermal expansion. In this context, we have calculated the anharmonic constants by using the following Helmholtz free energy F(T, V) equation that includes all the anharmonic terms [25,39,40],

$$\mathrm{F(T, V)} = \mathrm{F^{qh}(T, V)} + \mathrm{F^{anh}(T, V)} = \mathrm{F^{qh}(T, V)} + \mathrm{F_3(T, V)} + \mathrm{F_4(T, V)} \tag{6}$$

In this equation, the explicit anharmonic contribution $F^{anh}(T, V)$ is directly related to the higher order-crystal potential energy, and hence, $F^{anh}(T, V)$ can be considered as a perturbation term [39–41]. To calculate the anharmonic coefficient α_R from Raman modes, we have adapted the following equation [25]:

$$\alpha_R = \frac{-3nk_B}{E_T}\left[\gamma\left(\frac{\Delta V}{V}\right) + \left(\frac{\Delta\omega_j}{\omega_j}\right)\right]. \tag{7}$$

Here, we have estimated the Grüneisen parameters γ from temperature dependent Raman spectroscopy data by using the following equation [42]:

$$\gamma = -\frac{1}{\alpha_V\omega_0}\left(\frac{\Delta\omega}{\Delta T}\right)\Delta T, \tag{8}$$

where α_V represents the volumetric thermal expansion coefficient, ω_0 is the harmonic frequency and ΔT is the temperature difference, and $\frac{\Delta\omega}{\Delta T}$ is the first-order temperature coefficient. We have estimated the γ value from Eq. (8) and calculated the anharmonic coefficient α_R. The values of γ, and α_R estimated from Raman spectroscopy data are tabulated in Table II.

Similarly, the anharmonic coefficient from C_P measurements, denoted as α_{C_P}, can be evaluated from the temperature dependent C_P data. The value of measured C_P with temperature is depicted in Fig. 7(a). For calculating the α_{C_P} values, the following equation is used [11,43,44]:

$$\mathrm{C_P} = \mathrm{C_V^h} + \mathrm{C_V^{QH}} + \mathrm{C_V^{anh}} + \mathrm{C_V^{defects}} \tag{9}$$

where C_V^h, C_V^{QH}, C_V^{anh}, and $C_V^{defects}$ respectively are the harmonic, quasiharmonic, anharmonic, and defects contribution to C_P [43]. The quasiharmonic contribution C_V^{QH} can be written as $C_V^{QH} = B_M V\alpha_V^2 T$, where B_M is the bulk modulus, V is the molar volume, and α_V is the volumetric thermal expansion of the system. Similarly, $C_P^{defects}$ can be expressed as [45] $C_V^{defects} = Nk_b e^{\Delta S/k_B}(E/k_B T)^2 e^{E/k_B T}$. Here, ΔS and E, respectively, are the formation entropy and formation energy due to point defects in the Mg_3Sb_2 lattice, mostly due to Mg deficiency and dopant elements (Li). However, it was reported that the value of $C_V^{defects}$ contribution to C_P is almost negligible at room temperature and below [43]. Hence, three important factors namely harmonic, quasiharmonic, and anharmonic contributions dominate the C_P of a polycrystalline system. The anharmonic contribution C_V^{anh} can be written as $C_V^{anh} = -T\frac{\partial^2}{\partial T^2}(P_3 + P_4)$, where P_3, and P_4 are the first-order cubic and quartic terms of the free energy. Since, both the terms are directly proportional to T^2, hence for fitting the experimental temperature dependent C_P data, one term will be positive and another one will be negative. Therefore Eq. (9) can be rewritten as

$$\begin{aligned}\mathrm{C_P} &= \mathrm{C_V} + \mathrm{B_M V}\alpha_V^2\mathrm{T} - \mathrm{T}\frac{\partial^2}{\partial \mathrm{T}^2}(\mathrm{P_3} + \mathrm{P_4}) + \mathrm{C_V^{defects}} \\ &= \mathrm{C_V} + \mathrm{B_M V}\alpha_V^2\mathrm{T} + 3\mathrm{nk_B}\alpha_{C_P}\mathrm{T} + \mathrm{Nk_B}e^{\Delta S/k_B}.\end{aligned} \tag{10}$$

The experimental C_p is fitted using Eq. (10) to estimate the anharmonic term α_{C_P}. From the measured linear thermal coefficient values, the volumetric thermal expansion coefficient (α_V) can be estimated as $\alpha_V = 3\times$ linear thermal expansion

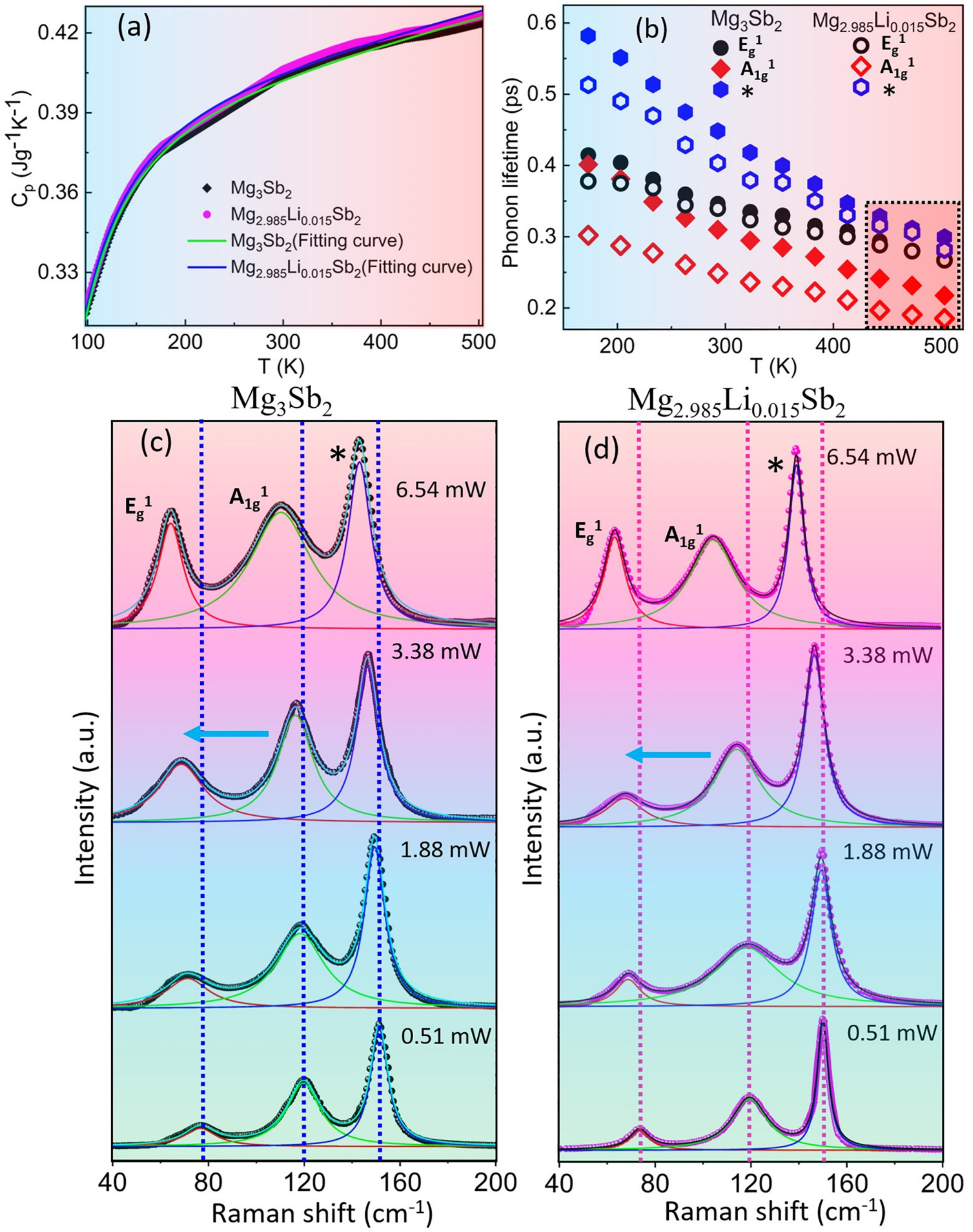

FIG. 7. (a) Estimated phonon lifetime of E_g^1, A_{1g}^1 and forbidden Raman modes for Mg_3Sb_2 and $Mg_{2.985}Li_{0.015}Sb_2$ samples. (b) Experimentally measured specific heat data along with the fitted curves of both samples. (c) Room-temperature Raman spectra collected at different laser power for Mg_3Sb_2. (d) Room-temperature Raman spectra collected at different laser power for $Mg_{2.985}Li_{0.015}Sb_2$.

coefficient [11]. The calculated volumetric thermal expansion coefficient values for Mg_3Sb_2, and $Mg_{2.985}Li_{0.015}Sb_2$ are found to be $65.7 \times 10^{-6}\ K^{-1}$, $65.8 \times 10^{-6}\ K^{-1}$, respectively. We have estimated the anharmonic coefficient α_{C_P} for $\alpha_{\mathrm{C_P}}$ for Mg_3Sb_2 and $Mg_{2.985}Li_{0.015}Sb_2$ samples by taking the reported bulk modulus values [46]. The values of α_{C_P} for undoped and Li-doped Mg_3Sb_2 are found to be $1.016 \times 10^{-4}\ K^{-1}$, and $1.019 \times 10^{-4}\ K^{-1}$, respectively. The anharmonic constants estimated from Raman spectroscopy as well as from specific heat data are nearly equal to each other (refer to Table III). However, as can be observed from Table I that the α_R value for A_{1g}^1 mode is higher than that for E_g^1, and forbidden modes, that confirms that longitudinal phonon mode contributes more anharmonicity in Mg_3Sb_2. The anharmonic coefficient values are higher when lighter atom "Li" is doped at the Mg1 site. From the above observations, it can be concluded that low lattice thermal conductivity in polycrystalline Mg_3Sb_2 is mostly due to its large phonon anharmonicity associated with the different bond strength associated lattice. The first term C_V in Eq. (10) is used to calculate the Grüneisen parameter (γ) using the $C_V = \alpha V B_M \gamma$ relation [47,48]. Table II summarizes the γ values estimated from

TABLE I. Calculated fitting parameters from the Raman spectra of undoped and Li doped Mg_3Sb_2 Samples in the temperature range 173–503 K.

Sample	E_g^1 peak	A_{1g}^1 peak	$*$/IR peak
Mg_3Sb_2	$\omega_o = 75.5$	$\omega_o = 122.193$	$\omega_o = 153.38$
	A = −0.25	A = −0.26	A = −0.22
	B = −0.005	B = −0.004	B=−0.007
	C = 0.17	C = 0.26	C = 0.21
	D = 0.007	D = 0.009	D = 0.008
$Mg_{2.985}Li_{0.015}Sb_2$	$\omega_o = 72.16$	$\omega_o = 121.57$	$\omega_o = 152.27$
	A = −0.24	A = −0.29	A = −0.23
	B = −0.004	B = −0.002	B = 0.003
	C = 0.19	C = 0.28	C = 0.23
	D = 0.0086	D = 0.012	D = 0.010

TABLE III. The estimated values of power coefficient ($\frac{\Delta\omega}{\Delta P}$) and lattice thermal conductivity (κ_{lattice}) of Mg_3Sb_2 and $Mg_{2.985}Li_{0.01}Sb_2$ samples.

Parameters	Mg_3Sb_2	$Mg_{2.985}Li_{0.015}Sb_2$
$\left(\frac{\Delta\omega}{\Delta P}\right)_{E_g^1}$	−1.92	−1.58
$\left(\frac{\Delta\omega}{\Delta P}\right)_{A_{1g}^1}$	−1.60	−1.98
$\left(\frac{\Delta\omega}{\Delta P}\right)_{*/IR}$	−1.39	−1.83
κ_{lattice} (estimated from Raman spectroscopy)	1.34	1.18
κ_{lattice} (from LFA measurement)	1.23	1.11

Raman spectroscopy, and specific heat data. It can be clearly observed from Table II that the value of γ is slightly higher in $Mg_{2.985}Li_{0.015}Sb_2$ sample compared to undoped Mg_3Sb_2. It concludes that even if Li is lighter than Mg, still Li doping at the Mg site helps to introduce more anharmonicity in Mg_3Sb_2 lattice, which might help to lower the lattice thermal conductivity in Li-doped Mg_3Sb_2 compared to that of undoped Mg_3Sb_2.

Next, we proceed to calculate the phonon lifetime, which is a signature of phonon propagation in a material, using energy-time uncertainty relation $\frac{\Gamma}{\hbar} = \frac{1}{\tau}$, where τ is the phonon lifetime, Γ is the experimentally measured FWHM in cm^{-1}, and $\hbar = h/2\pi = 5.3 \times 10^{-12}\, cm^{-1}s$ [49,50]. The τ is calculated in the temperature range 173–503 K and is visualized in Fig. 7(b). It can be clearly observed that the phonon lifetime of all-optical phonon modes decreases with increased temperature. The shorter phonon lifetime is a signature of phonon decay and hence low lattice thermal conductivity is expected in undoped and Li-doped Mg_3Sb_2 at higher temperatures. It can be perceived from Fig. 7(b) that, below 300 K, phonon lifetime of the forbidden mode is much higher than E_g^1 and A_{1g}^1 modes, which confirms dominance of forbidden mode for thermal transport in Mg_3Sb_2 at low temperature. Above 300 K, phonon lifetime of forbidden and A_{1g}^1 modes decreases at a higher rate than that of E_g^1 mode. The steady fall in phonon lifetime envisages the increase in phonon anharmonicity and decrease in κ_{lattice} in the Mg_3Sb_2 at higher temperatures. Above 400 K, the phonon lifetime of the transverse modes is found to be almost same, and longitudinal mode is having lowest phonon lifetime for both the samples [a dotted region in Fig. 7(b)]. Hence, it can be stated that in the case of polycrystalline Mg_3Sb_2, softening of longitudinal phonon mode is mostly responsible for the reduction in lattice thermal conductivity. From Figs. 5, 6, and 7(b), it might be confirmed that the large anharmonicity and low lattice thermal conductivity in Mg_3Sb_2 is mostly associated with the anharmonicity related to the Raman modes. To compare the experimentally measured lattice thermal thermal conductivity with the estimated values from Raman spectroscopy, the lattice thermal conductivity of Mg_3Sb_2 and $Mg_{2.985}Li_{0.015}Sb_2$ samples are calculated from the power- and temperature-dependent Raman modes. The fact that the Raman peak shift is associated with the thermal energy driven atoms/lattice vibrations, lattice thermal conductivity (κ_{lattice}) can be precisely evaluated from the radial heat flow according to the equation [51]

$$\kappa_{\text{lattice}} = \frac{\frac{\Delta\omega}{\Delta T}}{4\sqrt{\pi}\, r \frac{\Delta\omega}{\Delta P}}. \tag{11}$$

In Eq. (11), P is laser power, and r is radius of the objective aperture used in Raman spectroscopy measurements. The

TABLE II. The estimated values of Grüneisen parameter (γ) and anharmonic constant (α_R), of Mg_3Sb_2 and $Mg_{2.985}Li_{0.01}Sb_2$ samples and comparison with reported values available in the literature.

Parameters	Mg_3Sb_2	$Mg_{2.985}Li_{0.015}Sb_2$	Comparison
γ (from LFA)	1.93	2.12	1.83–2.6 [21,57]
γ (from Raman data)	1.49	1.53	1.83–2.6 [21,57]
γ (from C_p)	1.61	1.63	1.83–2.6 [21,57]
$\alpha_R(10^{-4}\,K^{-1})$	$3.75(rmE_g^1)$	$3.93(E_g^1)$	5.1 (SnSe) [33]
$\alpha_R(10^{-4}\,K^{-1})$	$4.3(A_{1g}^1)$	$4.5(A_{1g}^1)$	5.1 (SnSe) [33]
$\alpha_R(10^{-4}\,K^{-1})$	2.5($*$/IR)	2.83($*$/IR)	5.1 (SnSe) [33]
$\alpha_{C_p}(10^{-4}\,K^{-1})$	1.016	1.019	1.5 (SnSe) [33]
$\alpha_v(10^{-6}\,K^{-1})$	65.7	65.8	66.9 [11], 59.1 (PbTe) [58]

numerator term $\frac{\Delta\omega}{\Delta T}$ is the temperature coefficient, while the term $\frac{\Delta\omega}{\Delta p}$ in the denominator is the power coefficient. We have used a 50X objective lens for both temperature and power-dependent Raman measurements, which corresponds to the r value of $\sim 3\,\mu\mathrm{m}$. The value of $\frac{\Delta\omega}{\Delta T}$ can be derived from the temperature-dependent Raman peak position. The shift in Raman peaks with an increase in temperature is analyzed using the equation [52]: $\omega(\mathrm{T}) = \omega_0 + \alpha_1\mathrm{T} + \alpha_2\mathrm{T}^2$, where α_1 and α_2 respectively are the first- and second-order temperature coefficients of the Raman modes, and ω_0 is the harmonic frequency. The $\frac{\Delta\omega}{\Delta P}$ term is estimated from the shift in Raman peak position due to an increase in incident laser power. The room-temperature power-dependent Raman spectra for undoped and doped Mg_3Sb_2 samples are obtained at a different laser power of 0.093, 0.515, 1.88, and 3.38 mW, and is depicted in Fig. 7(b). It is observed from Fig. 7(b) that the Raman peak shifts towards a lower frequency region when laser power is increased. The shifting of the Raman peaks with an increase in laser power is analyzed by the equation [53,54]

$$\Delta\omega = \omega P_2 - \omega P_1 = \chi_P(P_2 - P_1) = \chi_P \Delta P, \qquad (12)$$

where ω is the Raman peak shift at different laser power, and χ_P represents the first-order power-dependent coefficient. To obtain power coefficient values, the power-dependent Raman peak shift for Mg_3Sb_2 and $Mg_{2.985}Li_{0.015}Sb_2$ samples are fitted with a linear function as per Eq. (12). The estimated power coefficient values for all Raman modes are tabulated in Table III. The lattice thermal conductivity of Mg_3Sb_2 and $Mg_{2.985}Li_{0.015}Sb_2$ samples are evaluated using Eq. (11) and is tabulated in Table III. We have also estimated the γ values from experimental lattice thermal conductivity data [6]. From the overall observation, it can be inferred that low lattice thermal conductivity observed in polycrystalline Mg_3Sb_2 does not follow the common mass law, $\kappa_\mathrm{lattice} \propto \mathrm{M}^{-1}$, and is entirely due to large phonon anharmonicity associated with the longitudinal and transverse phonon modes of the Mg_3Sb_2 lattice. The room-temperature lattice thermal conductivity values estimated from Raman spectroscopy data is found to be in good agreement with experimentally measured values. It can be noticed that the obtained lattice thermal conductivity values ~1.34 and 1.18 W/mK at 300 K for Mg_3Sb_2 and $Mg_{2.985}Li_{0.015}Sb_2$ samples are very low and nearly equal to that of the other heavy thermoelectric systems like SnSe and PbTe. It is to be noted that the lattice thermal conductivity value at 300 K for SnSe, PbTe, and Bi_2Te_3 TE system are ~0.76 W/mK in parallel direction (1.2 W/mK in transverse direction), 2.4 W/mK, and 1.38 W/mK, respectively [32,55,56]. From the optical phonon studies, it can be concluded that both three-phonon and four-phonon scattering help to enhance the phonon anharmonicity, which leads to the reduction in lattice thermal conductivity of lightweight Mg_3Sb_2 thermoelectric system.

IV. SUMMARY

A comprehensive investigation employing temperature-dependent Raman spectroscopy was conducted to unravel the large phonon anharmonicity and low lattice thermal conductivity in both undoped and Li-doped Mg_3Sb_2. By utilizing temperature-dependent Raman spectroscopy in tandem with experimental heat capacity data, the phonon anharmonicity in polycrystalline Mg_3Sb_2 was thoroughly assessed. By comparing the Raman modes of undoped Li-doped Mg_3Sb_2 with that from Sb powder, it was revealed that three Raman modes observed in Mg_3Sb_2 are indeed from the Mg_3Sb_2 lattice. Further analysis revealed a softening trend in the Raman modes at elevated temperatures, denoting an augmented level of phonon anharmonicity in light-weight Mg_3Sb_2. Notably, it was observed that the A^1_{1g} phonon mode contributed more to the phonon anharmonicity compared to the other two phonon modes. Polarized Raman spectroscopy data unveiled a twofold lattice symmetry, confirming the anisotropic nature of Mg_3Sb_2. This anisotropy remained apparent at lower temperatures in both undoped and Li-doped Mg_3Sb_2. Interestingly, in undoped Mg_3Sb_2, the lattice symmetry axis was consistent across all the phonon modes. In contrast, the symmetry axis of all the optical phonon modes varied in Li-doped Mg_3Sb_2, indicating the tailored symmetry axis in Mg_3Sb_2 through doping. This alteration might contribute to the higher phonon anharmonicity observed in Li-doped Mg_3Sb_2. The concurrent decrease in phonon lifetime with rising temperatures indicated a phonon decay and a reduction in lattice thermal conductivity at elevated temperatures. The anharmonic contributions estimated from the temperature-dependent Raman modes corroborate the presence of quasi-anharmonic volume expansion along with three-phonon and four-phonon scatterings. The lattice thermal conductivity assessed from the optical phonon modes and specific heat aligned closely with the experimentally measured values, substantiating the applicability of Raman spectroscopy in estimating the lattice thermal conductivity of undoped and doped Mg_3Sb_2. The findings substantially contribute to the understanding of the pronounced phonon anharmonicity in lightweight Mg_3Sb_2 system, which is mainly due to the contribution from the three-phonon and four-phonon scattering mechanisms as well as quasiharmonic volume expansion, Overall, the observed low lattice thermal conductivity in the lightweight Mg_3Sb_2 thermoelectric system challenges the common mass law of lattice thermal conductivity, $\kappa_\mathrm{lattice} \propto \mathrm{M}^{-1}$ and is closely linked to the substantial phonon anharmonicity associated with the Mg_3Sb_2 lattice due to thermal expansion and phonon-phonon anharmonicity.

ACKNOWLEDGMENTS

M.B. acknowledges the financial support received from Ministry of Science and Technology, India through the Core Research Grant scheme (CRG/2022/005539). D.K.S. acknowledges the financial support from Ministry of Human Research and Developments (MHRD), India through IMPRINT-I scheme. The authors are grateful to Department of Physics, IIT Madras for providing the Physical Properties Measurement System (make M/S Quantum Design, USA) facility.

[1] D. M. Rowe, *CRC Handbook of Thermoelectrics: Macro to Nano* (CRC Press, Boca Raton, FL, 2006).

[2] J. Zhang, L. Song, and B. B. Iversen, Probing efficient *n*-type lanthanide dopants for Mg_3Sb_2 thermoelectrics, Adv. Sci. **7**, 2002867 (2020).

[3] O. Delaire, J. Ma, K. Marty, A. F. May, M. A. McGuire, M.-H. Du, D. J. Singh, A. Podlesnyak, G. Ehlers, M. D. Lumsden, and B. C. Sales, Giant anharmonic phonon scattering in PbTe, Nat. Mater. **10**, 614 (2011).

[4] M. Dimitrievska, A. Fairbrother, E. Saucedo, A. Perez-Rodriguez, and V. Izquierdo-Roca, Influence of compositionally induced defects on the vibrational properties of device grade $Cu_2ZnSnSe_4$ absorbers for kesterite based solar cells, Appl. Phys. Lett. **106**, 073903 (2015).

[5] J. Ding, T. Lanigan-Atkins, M. Calderón-Cueva, A. Banerjee, D. L. Abernathy, A. Said, A. Zevalkink, and O. Delaire, Soft anharmonic phonons and ultralow thermal conductivity in $Mg_3(Sb, Bi)_2$ thermoelectrics, Sci. Adv. **7**, eabg1449 (2021).

[6] M. Tiadi, M. Battabyal, P. K. Jain, A. Chauhan, D. K. Satapathy, and R. Gopalan, Enhancing the thermoelectric efficiency in *p*-type Mg_3Sb_2 via Mg site co-doping, Sustain. Energy Fuels **5**, 4104 (2021).

[7] M. Tiadi, V. Trivedi, S. Kumar, P. K. Jain, S. K. Yadav, R. Gopalan, D. K. Satapathy, and M. Battabyal, Enhanced thermoelectric efficiency in *p*-type Mg_3Sb_2: Role of monovalent atoms codoping at Mg sites, ACS Appl. Mater. Interfaces. **15**, 20175 (2023).

[8] V. Trivedi, M. Tiadi, B. S. Murty, D. K. Satapathy, M. Battabyal, and R. Gopalan, Giant thermoelectric efficiency of single-filled skutterudite nanocomposites: Role of interface carrier filtering, ACS Appl. Mater. Interfaces **14**, 51084 (2022).

[9] P. Balasubramanian, M. Battabyal, D. Sivaprahasam, and R. Gopalan, On the formation of phases and their influence on the thermal stability and thermoelectric properties of nanostructured zinc antimonide, J. Phys. D: Appl. Phys. **50**, 015602 (2017).

[10] M. Battabyal, B. Priyadarshini, D. Sivaprahasam, N. S. Karthiselva, and R. Gopalan, The effect of Cu_2O nanoparticle dispersion on the thermoelectric properties of *n*-type skutterudites, J. Phys. D: Appl. Phys. **48**, 455309 (2015).

[11] M. T. Agne, K. Imasato, S. Anand, K. Lee, S. K. Bux, A. Zevalkink, A. J. E. Rettie, D. Y. Chung, M. G. Kanatzidis, and G. J. Snyder, Heat capacity of Mg_3Sb_2, Mg_3Bi_2, and their alloys at high temperature, Mater. Today Phys. **6**, 83 (2018).

[12] M. Wu, H. Yang, F. Xie, and L. Huang, Lattice thermal conductivity in XMg_2Sb_2 (X = Ca or Mg) compounds: Temperature and high-order anharmonicity effect, Materials **16**, 7349 (2023).

[13] X. Ma, H. Yao, S. Zhi, P. Zhao, S. Ye, S. Duan, L. Yin, J. Li, X. Bao, J. Sui, F. Cao, Q. Zhang, and J. Mao, Identifying the point defects in single-crystalline Mg_3Sb_2, Chem. Mater. **35**, 5640 (2023).

[14] A. Bhardwaj, A. K. Shukla, S. R. Dhakate, and D. K. Misra, Graphene boosts thermoelectric performance of a Zintl phase compound, RSC Adv. **5**, 11058 (2015).

[15] T. Kanno, H. Tamaki, M. Yoshiya, H. Uchiyama, S. Maki, M. Takata, and Y. Miyazaki, High-density Frenkel defects as origin of *n*-type thermoelectric performance and low thermal conductivity in Mg_3Sb_2-based materials, Adv. Fun. Mater. **31**, 2008469 (2021).

[16] D. Das, S. Das, P. Singha, K. Malik, A. K. Deb, A. Bhattacharyya, V. A. Kulbachinskii, R. Basu, S. Dhara, S. Bandyopadhyay, and A. Banerjee, Evolution of phonon anharmonicity in Se-doped Sb_2Te_3 thermoelectrics, Phys. Rev. B **96**, 064116 (2017).

[17] M. Battabyal, B. Priyadarshini, L. Pradipkanti, D. K. Satapathy, and R. Gopalan, Phase stability and lattice thermal conductivity reduction in $CoSb_3$ skutterudites, doped with chalcogen atoms, AIP Adv. **6**, 075308 (2016).

[18] Z. Zhao, J. Elwood, and M. A. Carpenter, Phonon anharmonicity of PdO studied by Raman spectrometry, J. Phys. Chem. C **119**, 23094 (2015).

[19] S. Kumar, M. Battabyal, K. Sethupathi, and D. K. Satapathy, Thermoelectric properties of Ag-doped CuI: A temperature dependent optical phonon study, Phys. Chem. Chem. Phys. **24**, 24228 (2022).

[20] M. Tiadi, D. K. Satapathy, and M. Battabyal, Evolution of optical phonon modes and thermoelectric properties in doped Bi_2Te_3: A temperature-dependent Raman spectroscopy study, Phys. Rev. Mater. **7**, 015401 (2023).

[21] W. Peng, G. Petretto, G.-M. Rignanese, G. Hautier, and A. Zevalkink, An unlikely route to low lattice thermal conductivity: Small atoms in a simple layered structure, Joule **2**, 1879 (2018).

[22] J.-i. Tani, M. Takahashi, and H. Kido, Lattice dynamics and elastic properties of Mg_3As_2 and Mg_3Sb_2 compounds from first-principles calculations, Phys. B: Condens. Matter **405**, 4219 (2010).

[23] D. L. Rousseau, R. P. Bauman, and S. P. S. Porto, Normal mode determination in crystals, J. Raman Spectrosc. **10**, 253 (1981).

[24] W. Richter and C. R. Becker, A Raman and far-infrared investigation of phonons in the rhombohedral $V_2 - VI_3$ compounds Bi_2Te_3, Bi_2Se_3, Sb_2Te_3 and $Bi_2(Te_{1-x}Sex)_3(0 < x < 1)$, $(Bi_{1-y}Sby)_2Te_3(0 < y < 1)$, Phys. Status Solidi B **84**, 619 (1977).

[25] M. Jin, S. Lin, W. Li, X. Zhang, and Y. Pei, Nearly isotropic transport properties in anisotropically structured *n*-type single-crystalline Mg_3Sb_2, Mater. Today Phys. **21**, 100508 (2021).

[26] Q.-H. Tan, Y.-M. Li, J.-M. Lai, Y.-J. Sun, Z. Zhang, F. Song, C. Robert, X. Marie, W. Gao, P.-H. Tan, and J. Zhang, Quantum interference between dark-excitons and zone-edged acoustic phonons in few-layer WS_2, Nat. Commun. **14**, 88 (2023).

[27] G. S. Duesberg, I. Loa, M. Burghard, K. Syassen, and S. Roth, Polarized Raman spectroscopy on isolated single-wall carbon nanotubes, Phys. Rev. Lett. **85**, 5436 (2000).

[28] Q. Song, X. Pan, H. Wang, K. Zhang, Q. Tan, P. Li, Y. Wan, Y. Wang, X. Xu, M. Lin, X. Wan, F. Song, and L. Dai, The in-plane anisotropy of WTe_2 investigated by angle-dependent and polarized Raman spectroscopy, Sci. Rep. **6**, 29254 (2016).

[29] X. Zhou, X. Hu, B. Jin, J. Yu, K. Liu, H. Li, and T. Zhai, Highly anisotropic GeSe nanosheets for phototransistors with ultrahigh photoresponsivity, Adv. Sci. **5**, 1800478 (2018).

[30] H. Zobeiri, N. Hunter, R. Wang, X. Liu, H. Tan, S. Xu, and X. Wang, Thermal conductance between water and nm-thick WS_2: Extremely localized probing using nanosecond energy transport state-resolved Raman, Nanoscale Adv. **2**, 5821 (2020).

[31] M. Balkanski, R. F. Wallis, and E. Haro, Anharmonic effects in light scattering due to optical phonons in silicon, Phys. Rev. B **28**, 1928 (1983).

[32] Y. Li, X. Shi, D. Ren, J. Chen, and L. Chen, Investigation of the anisotropic thermoelectric properties of oriented polycrystalline SnSe, Energies **8**, 6275 (2015).

[33] F. Liu, P. Parajuli, R. Rao, P. C. Wei, A. Karunarathne, S. Bhattacharya, R. Podila, J. He, B. Maruyama, G. Priyadarshan, J. R. Gladden, Y. Y. Chen, and A. M. Rao, Phonon anharmonicity in single-crystalline SnSe, Phys. Rev. B **98**, 224309 (2018).

[34] S. R. Popuri, M. Pollet, R. Decourt, M. L. Viciu, and J. W. G. Bos, Evidence for hard and soft substructures in thermoelectric SnSe, Appl. Phys. Lett. **110**, 253903 (2017).

[35] Y. Tian, G. B. Osterhoudt, S. Jia, R. J. Cava, and K. S. Burch, Local phonon mode in thermoelectric Bi_2Te_2Se from charge neutral antisites, Appl. Phys. Lett. **108**, 041911 (2016).

[36] P. G. Klemens, Anharmonic decay of optical phonons, Phys. Rev. **148**, 845 (1966).

[37] A. Das, A. Chauhan, V. Trivedi, M. Tiadi, R. Kumar, M. Battabyal, and D. K. Satapathy, Effect of iodine doping on the electrical, thermal and mechanical properties of SnSe for thermoelectric applications, Phys. Chem. Chem. Phys. **23**, 4230 (2021).

[38] P. B. Allen, Theory of thermal expansion: Quasi-harmonic approximation and corrections from quasi-particle renormalization, Mod. Phys. Lett. B **34**, 2050025 (2020).

[39] A. Leadbetter, Anharmonic effects in the thermodynamic properties of solids II. Analysis of data for lead and aluminium, J. Phys. C: Solid State Phys. **1**, 1489 (1968).

[40] T. H. K. Barron, Interatomic potentials in ideal anharmonic crystals, Disc. Faraday Soc. **40**, 69 (1965).

[41] D. M. T. Newsham, Anharmonic contributions to the heat capacities of silicon and germanium, Phys. Rev. **152**, 841 (1966).

[42] N. Suss, A. Ritscher, M. Lerch, and I. Efthimiopoulos, Anharmonic effects in ordered kesterite-type Cu_2ZnSnS_4, Solids **2**, 385 (2021).

[43] P. Jund, R. Viennois, X. Tao, K. Niedziolka, and J.-C. Tédenac, Physical properties of thermoelectric zinc antimonide using first-principles calculations, Phys. Rev. B **86**, 019901(E) (2012).

[44] C. R. Brooks and R. E. Bingham, The specific heat of aluminum from 330 to 890 K and contributions from the formation of vacancies and anharmonic effects, J. Phys. Chem. Solids **29**, 1553 (1968).

[45] R. C. Shukla and C. A. Plint, Anharmonic effects in the specific heat of aluminum, Int. J. Thermophys. **1**, 299 (1980).

[46] J. Li, S. Zhang, B. Wang, S. Liu, L. Yue, G. Lu, and S. Zheng, Designing high-performance *n*-type Mg_3Sb_2-based thermoelectric materials through forming solid solutions and biaxial strain, J. Mater. Chem. A **6**, 20454 (2018).

[47] J. J. Gilvarry, The Lindemann and Grüneisen laws, Phys. Rev. **102**, 308 (1956).

[48] D. T. Morelli, V. Jovovic, and J. P. Heremans, Intrinsically minimal thermal conductivity in cubic $\mathrm{I-V-VI_2}$ semiconductors, Phys. Rev. Lett. **101**, 035901 (2008).

[49] L. Bergman, D. Alexson, P. L. Murphy, R. J. Nemanich, M. Dutta, M. A. Stroscio, C. Balkas, H. Shin, and R. F. Davis, Raman analysis of phonon lifetimes in AlN and GaN of wurtzite structure, Phys. Rev. B **59**, 12977 (1999).

[50] M. Alam, K. H. Gooen, B. D. Bartolo, A. Linz, E. Sharp, L. Gillespie, and G. Janney, Optical spectra and laser action of neodymium in a crystal $Ba_2MgGe_2O_7$, J. Appl. Phys. **39**, 4728 (1968).

[51] P. Xiao, E. Chavez-Angel, S. Chaitoglou, M. Sledzinska, A. Dimoulas, C. M. S. Torres, and A. E. Sachat, Anisotropic thermal conductivity of crystalline layered $SnSe_2$, Nano Lett. **21**, 9172 (2021).

[52] D. Park, S. Park, K. Jeong, H.-S. Jeong, J. Y. Song, and M.-H. Cho, Thermal and electrical conduction of single-crystal Bi_2Te_3 nanostructures grown using a one step process, Sci. Rep. **6**, 19132 (2016).

[53] R. Yan, J. R. Simpson, S. Bertolazzi, J. Brivio, M. Watson, X. Wu, A. Kis, T. Luo, A. R. Hight Walker, and H. G. Xing, Thermal conductivity of monolayer molybdenum disulfide obtained from temperature-dependent Raman spectroscopy, ACS Nano **8**, 986 (2014).

[54] X. Gong, Y. Wang, Q. Hong, J. Liu, C. Yang, H. Zou, Y. Zhou, D. Huang, H. Wu, Z. Zhou, B. Zhang, and X. Zhou, *In-situ* micro-Raman study of SnSe single crystals under atmosphere: Effect of laser power and temperature, Spectrochim. Acta A: Mol. Biomol. Spectrosc. **265**, 120375 (2022).

[55] L.-D. Zhao, S.-H. Lo, Y. Zhang, H. Sun, G. Tan, C. Uher, C. Wolverton, V. P. Dravid, and M. G. Kanatzidis, Ultralow thermal conductivity and high thermoelectric figure of merit in SnSe crystals, Nature (London) **508**, 373 (2014).

[56] Z. Zhang, M. Sun, J. Liu, L. Cao, M. Su, Q. Liao, Y. Deng, and L. Qin, Ultra-fast fabrication of Bi_2Te_3 based thermoelectric materials by flash-sintering at room temperature combining with spark plasma sintering, Sci. Rep. **12**, 10045 (2022).

[57] J. Zhang, L. Song, M. Sist, K. Tolborg, and B. B. Iversen, Chemical bonding origin of the unexpected isotropic physical properties in thermoelectric Mg_3Sb_2 and related materials, Nat. Commun. **9**, 4716 (2018).

[58] O. Madelung, *Semiconductors: Data Handbook* (Springer-Verlag, Berlin, Heidelberg, 2004).